CO$_2$ hydrogenation over 5%Ni/CeO$_2$–Al$_2$O$_3$ catalysts: effect of supports composition

Amir Mosayebi[1] · Atieh Ranjbar[1] · Mohammad Hosein Eghbal Ahmadi[1]

Abstract

In current work, the investigation centered on assessing the impact of the CeO$_2$ to Al$_2$O$_3$ ratio in a 5%Ni/CeO$_2$–Al$_2$O$_3$ catalyst on the CO$_2$ hydrogenation reaction within the temperature range of 240–400 °C. The primary aim was to achieve enhanced conversion rates, while minimizing coke deposition on the catalyst surface. Nickel was incorporated into the CeO$_2$–Al$_2$O$_3$ supports via the deposition–precipitation method. The various physicochemical properties of fresh, reduced and spent catalysts were studied using techniques such as thermal gravimetric analysis (TGA), X-ray diffraction (XRD), N$_2$ adsorption/desorption, temperature programmed reduction (TPR), H$_2$-chemisorption, X-ray fluorescence (XRF), and CHNS analyzer. XRD results revealed that the addition of CeO$_2$ to the Ni/Al$_2$O$_3$ catalyst and the increase in ceria loading in the hybrid support had no obvious effect on the crystalline structure. However, several properties including reducibility, coke deposition, and coke formation quantity, coke structure on the catalyst surface, catalytic performance, and thermal stability were altered. The CO$_2$ conversion remained relatively stable (41.25%) up to 35 h initial on stream for Ni/Al$_2$O$_3$ catalyst, indicating no significant deactivation. Conversely, Ni/CeO$_2$–Al$_2$O$_3$ catalyst exhibited high stability up to 45 h initial. The highest CO$_2$ conversion (58%) was achieved with the Ni/CeO$_2$ (50%)–Al$_2$O$_3$ (50%) at 400 °C, primarily attributed to a lower interaction between nickel species and the support, along with a higher reduction degree. Ni/CeO$_2$–Al$_2$O$_3$ catalysts displayed higher methane selectivity and lower CO selectivity compared to both Ni/Al$_2$O$_3$ and Ni/CeO$_2$ catalysts across the entire temperature range of 240–400 °C.

Keywords CO$_2$ hydrogenation · Coke deposition · Stability · Selectivity · Ni/CeO$_2$–Al$_2$O$_3$

✉ Amir Mosayebi
mosayebi@tafreshu.ac.ir

[1] Department of Chemical Engineering, Tafresh University, Tafresh 39518 79611, Iran

Introduction

The continuous increase in carbon dioxide levels resulting from the burning of fossil fuels and its irreversible impact on the global climate cannot be neglected [1–3]. The concentration of atmospheric CO_2 reached 417.1 parts per million (ppm) in 2022, marking a 48% increase compared to pre-industrial levels of 280 ppm [4]. Despite efforts, less than 55% of emitted carbon dioxide is absorbed by plants and oceans through the photosynthesis cycle, leaving the remainder in the atmosphere [5, 6]. To address this challenge, the utilization of CO_2 through catalytic hydrogenation reactions has emerged as a promising approach [7]. By reacting thermodynamically stable CO_2 with high energy H_2, valuable chemicals and fuels can be produced [8]. Among the hydrogenation reactions, CO_2 methanation and reverse water–gas shift (RWGS) have garnered remarkable attention in recent years. RWGS reaction produces highly reactive CO from CO_2, serving as a feedstock for many industrial processes [9, 10]. CO_2 methanation or Sabatier reaction, converts abundant CO_2 into CH_4. CO_2 methanation and RWGS reactions have been widely studied in NASA projects for production of fuel and water from Martian atmospheric CO_2 [11]. CO_2 methanation also applied in power-to-gas technologies. In these technologies, the renewable hydrogen reacts with CO_2 from power plants (or industrial process) to produce storable methane [12]. The various metals including Pt [11, 12], Au [13], Ru [14], and Pd [7] have been applied for CO_2 hydrogenation reactions. However, these active metals are costly and less economically viable compared to Cu [15], Ni [16–19] and Co [20, 21]. Ni-based catalysts are extensively employed for hydrogenation reactions due to their acceptable catalytic performance and cost-effectiveness. However, nickel suffers from agglomeration, sintering and coke accumulation. Factors such as catalyst support, catalyst preparation method, Ni particle size and loading, and addition of promoter significantly affect the activity and selectivity of Ni catalysts [22, 23]. The choice of catalyst support plays a main role in determining catalytic activity, affecting factors such as active metal dispersion, crystal structure, and formation of inactive spinel phases. The nickel catalysts were supported on Al_2O_3 [24], SiO_2 [25], SBA-15 [26], CeO_2 [19–24], MgO [27], and perovskite [28] for CO_2 hydrogenation reactions. Al_2O_3 is commonly used as a support because of its low price, high surface area, porous structure, and excellent thermal stability, resulting in high catalytic performance [23]. Dekkar et al. [29] described that Ni/Al_2O_3 catalyst presented a synergistic effect between the various phases nickel oxide and $NiAl_2O_4$ formed during the catalyst synthesis method because of the various interactions between metal and support, which lead to increase in dispersion and stabilization of NiO species. Therefore, Ni/Al_2O_3 catalyst exhibited proper textural properties and superior catalytic activity in term of conversion, selectivity and stability in dry reforming of methane [29]. Al_2O_3 with its high surface area is capable to increase the Ni dispersion and consequently decrease nickel crystal size. However, Al_2O_3 promote coke formation and sintering of active metal particles, especially at high loadings due to its inherently acidic nature [28]. Dekkar et al. [29] founded that despite the coke deposition on the Ni/Al_2O_3, catalyst

showed a superior stability up to 66 h initial time on stream, which can be related to type of formed coke and the delocalization of the nickel active sites. To address these challenges, alkaline and transition metal oxides are often added to catalysts supported on Al_2O_3 to decrease coke formation and sintering [29–33]. The addition of basic material to acidic supports facilitates adsorption of reactant CO_2 and desorption of products [34–36]. Liang et al. [12] concluded that the addition of Sr and Ba to Ni/Al_2O_3 catalyst increases catalytic performance and shift the reaction towards CO_2 methanation. They concluded that effect of promoters on the reduction degree of nickel species is the main reason for their higher catalytic activity. CeO_2, an alkaline oxide known for its redox properties and oxygen vacancies, is extensively used as a support or promoter due to its favorable characteristics [37]. Wu et al. [38] synthesized Ni–CeO_2–Al_2O_3 catalysts using a one-pot sol–gel method. They illustrated that physical and chemical properties of synthesized catalysts influenced the carbon dioxide adsorption capacity on various crystal planes of cerium oxide, with the order of {110} > {100} > {111}. Thus, catalysts supported on CeO_2 exhibited distinct CO_2 hydrogenation capabilities due to exposure to different crystal planes. In the study of Xu et al. [39], CeCo catalysts with various mole ratios of cerium to cobalt were synthesized via a hard-template approach and their performance were evaluated in CO_2 catalytic hydrogenation reaction. The catalyst with a Ce/Co mole ratio of 0.5 exhibited a more homogeneous bimodal mesoporous distribution, leading to suitable conditions for the formation of surface oxygen vacancies and the effective dispersion of metallic cobalt. The methane selectivity of 100% obtained from the CeCo catalyst with mole ratio of cerium to cobalt of 0.5. This catalyst exhibited the maximum CO_2 conversion, which can be attributed to the formed oxygen vacancies, high surface area, high cobalt dispersion, and bimodal mesoporous structure. Additionally, the addition of CeO_2–Al_2O_3 can also decrease the acidity of alumina and mitigate its negative effects [40]. De piano et al. [41] used Ce as promoter for Ni/Al_2O_3 catalyst. The catalysts were prepared via successive and simultaneous impregnation techniques by keeping the Ce + Ni loading between 10 and 30 wt.%. They concluded that catalysts prepared by simultaneous method showed higher reducibility and basic sites due to Ni–O–Ce solid solutions and oxygen vacancies Therefore, the catalyst containing 15 wt.% Ce and 15 wt.% Ni prepared with simultaneous method showed highest catalytic activity (60% CO_2 conversion at 400 °C). The only disadvantage of CeO_2 catalysts compared to alumina catalysts is their lower specific surface area. Although, by using the appropriate synthesis method like hydrothermal [41], hard and soft template precipitation methods [41], and etc., this problem can be solved. Thus, Ni supported on mixed Al_2O_3–CeO_2 catalysts are expected to have high dispersion, high thermal stability, enhanced metal-support interactions, and redox properties.

In present research, Ni/Al_2O_3, Ni/CeO_2 and Ni/Al_2O_3–CeO_2 catalysts were synthesized with the various ratios of CeO_2 to Al_2O_3. The Al_2O_3, CeO_2, Al_2O_3–CeO_2 supports and catalysts containing 5 wt.% Ni were synthesized via deposition–precipitation method. The physicochemical properties of the fresh, reduced and spent catalysts were characterized using various techniques such as H_2-chemisorption, XRF, XRD, CHNS analyzer, N_2 adsorption–desorption, TPR, TGA and EA tests,

and their results were compared with each other's. Also, the catalytic activity (CO_2 conversion, CO selectivity and methane selectivity) and stability of spent catalysts were evaluated in CO_2 hydrogenation within the temperature range of 240–400 °C.

Experimental

Synthesis

CeO_2–Al_2O_3 support was synthesized using the precipitation technique. Initially, a specific amount of γ-Al_2O_3 (purchased from Sigma-Aldrich) was dispersed in a solution of cerium nitrate hexahydrate and stirred for 1 h (weight percentages of cerium oxide in the support were 0, 10, 30, 50 and 100). Subsequently, 1 molar NH_3 solution (10 mL) was gradually added drop-wise with stirring for 2 h at room temperature until pH reached 9. The resulting precipitate was filtered, washed with deionized water, and dried in a vacuum oven at 100 °C for 8 h. Finally, the sample was calcined at 600 °C for 6 h in a furnace. Nickel catalysts supported on the CeO_2–Al_2O_3 supports were synthesized using the deposition–precipitation method. The synthesis procedure for catalysts supported on the ceria and alumina were similar to that for the hybrid support of CeO_2–Al_2O_3. Firstly, the supports were added to a solution of nickel (II) nitrate hexahydrate and dispersed ultrasonically for 1 h. 1 molar solution of sodium borohydride was then added drop-wise to the solution and stirred for 6 h. The samples were separated, washed, and dried in a vacuum oven at 100 °C for 10 h. Finally, the catalysts were calcined at 500 °C for 6 h. Ni/γ-Al_2O_3, Ni/CeO_2 (10 wt.%)-Al_2O_3, Ni/CeO_2 (30 wt.%)-Al_2O_3, Ni/CeO_2 (50 wt.%)-Al_2O_3 and Ni/CeO_2 Catalysts were nominated as NA, NCA10, NCA30, NCA50 and NC, respectively. It should be noted that NA and NC catalysts were synthesized by same method with Ni/ CeO_2–Al_2O_3 catalysts. The nickel loading was 5 wt.% in all synthesized catalysts. The mass of nickel precursor in all the synthesized catalysts was 0.1 g. The mass of cerium nitrate hexahydrate for NC, NCA10, NCA30 and NCA50 were 1, 0.1, 0.3 and 0.5 g, respectively.

Characterization

XRF test was conducted via a WDXRF S8 Tiger Bruker to measure the actual content of nickel oxide in both the fresh and spent catalysts. The textural properties of the catalysts were assessed through N_2 adsorption–desorption measurements using a Tri StarII3020 apparatus. Prior to the testing, sample was degassed under nitrogen gas at 4000 °C for 4 h. specific surface area was determined using the Brunauer–Emmett–Teller (BET) method, while the average pore size and pore volume were calculated from the desorption branch of the isotherm using the Barrett–Joyner–Halenda (BJH) approach. The X-ray diffraction (XRD) patterns of calcined, reduced and spent catalysts were obtained using an XRD Philips PW1730 instrument. The diffraction profiles were recorded in the range of 20° to 90° at a scanning rate of 8°/min. Joint committee on powder diffraction standards (JCPDS)

database was utilized to identify the crystal phases present in the XRD patterns of the catalysts. TPR test was performed using a Quantachrome Chem BET 3000 TPR/TPD apparatus. Before the treatment, the catalysts were purged with argon gas at 220 °C and atmospheric pressure for 0.5 h. The catalyst temperature was then declined to 25 °C, and then gradually augmented to 1000 °C at a heating rate of 10 °C/min, while hydrogen flowed at 20 mL/min. To measure H$_2$ consumption amounts, the apparatus was calibrated via AgO$_2$ reduction as the reference material. The reduction degree of the catalysts was directly related to the amount of the hydrogen consumption. The amount of chemisorbed hydrogen on the catalysts was measured using an AMI-300 chemisorption analyzer-altamira instruments. After the reduction treatment, the sample temperature was decreased to 100 °C using a hydrogen stream. Then hydrogen stream was switched to argon gas at same temperature for 0.5 h to remove any adsorbed hydrogen. Afterwards, temperature programmed desorption (TPD) analysis was conducted by ramping up the temperature to 400 °C at a rate of 10 °C/min using an argon gas stream. The TPD profile was used to determine the Ni dispersion and average particle size. The thermal stability of the spent catalysts in CO$_2$ hydrogenation was investigated using a Rigaku TG 812 instrument. The spent catalysts were degassed with a nitrogen gas stream at a volumetric flow rate of 15 mL/h. The catalyst surface temperature was then raised to 1000 °C using an air stream to oxidize any deposited coke. The EuroEA3000-Single apparatus was employed to analyze the carbon and hydrogen content in the deposited coke, and the amount of coke on the spent catalyst was determined using a CHNS Analyzer (EMA 502 Elemental Analyzer).

Catalytic reaction

A fixed bed reactor with an inner diameter of 12 mm was utilized for conducting the catalytic reaction employing a 0.4 g catalyst with a particle size ranging from 90 to 160 μm. The catalyst was positioned in the center of the reactor using quartz wool pulgs, and the entire reactor was insulated with thermal insulation materials. Heating was achieved through an external electric furnace. The temperature control across different zones of the reactor, including the inlet, catalyst bed and outlet was maintained using three thermocouples. Prior to the reaction, the catalyst was reduced at 420 °C for 2 h under a hydrogen gas flow rate of 25 mL/min. Subsequently, the reactor temperature was lowered to 240 °C, while sustaining the hydrogen stream. The reactants, carbon dioxide gas followed by hydrogen, were introduced into the reactor, with their flow rates being measured and controlled via a mass flow controller (MFC). Experimental runs were conducted at varying reaction temperatures ranging from 240 to 400 °C. The total volume flow rate of the feed gas was set at 25 mL/min. The molar ratio of H$_2$/CO$_2$ was 4 in the inlet feed, thereby, volume flow rate of hydrogen and carbon dioxide in the reactants were 20 and 5 mL/min, respectively. Each experimental condition was tested three times to ensure reproducibility. Analysis of the reaction products was carried out using a Varian CP-3800 gas chromatograph to determine their compositions accurately.

The CO_2 conversion, CH_4 selectivity and CO selectivity was measured based on below relations.

$$CO_2 \text{ conversion } (\%) = \frac{n_{CO_2, \text{ in}} - n_{CO_2, \text{ out}}}{n_{CO_2, \text{ in}}} \times 100 \tag{1}$$

$$CO \text{ selectivity}(\%) = \frac{n_{CO,\text{out}}}{(n_{CH_4,\text{out}}) + (n_{CO,\text{out}})} \times 100 \tag{2}$$

$$CH_4 \text{selectivity}(\%) = \frac{n_{CH_4,\text{out}}}{(n_{CH_4,\text{out}}) + (n_{CO,\text{out}})} \times 100 \tag{3}$$

where $n_{CO_2,\text{in}}$, $n_{CO_2,\text{out}}$, $n_{CO,\text{out}}$ and $n_{CH_4,\text{out}}$ indicated to molar flow rate of CO_2 in inlet feed, molar flow rate of CO_2 in outlet, molar flow rate of CO in outlet and molar flow rate of methane in outlet.

Results and discussion

Catalysts characterization

Chemical analysis (XRF)

The weight percentages of nickel oxide in all fresh catalysts were 5 wt.%. XRF test was employed to validate the content of nickel oxide, and the results were shown

Table 1 The physicochemical properties of the catalysts

Catalyst	NiO (wt.%)[a]	Coke amount (wt.%)[b]	Surface area (m^2 g^{-1})[c]	Pore volume (cm^3 g^{-1})[d]	Mean pore size (nm)[d]
fresh NA	4.91	–	151.32	0.49	6.13
Spent NA	–	9.8	124.45	0.44	4.64
fresh NC	4.92	–	175.34	0.56	6.45
Spent NC	–	9.1	157.54	0.52	5.12
fresh NCA10	4.89	–	158.76	0.53	6.24
spent NCA10	–	8.4	143.25	0.49	5.87
fresh NCA30	4.92	–	163.47	0.55	6.13
Spent NCA30	–	7.8	153.56	0.51	5.97
fresh NCA50	4.94	–	169.47	0.52	5.87
Spent NCA50	–	7.1	162.45	0.49	5.58

[a]Measured by the XRF method

[b]Determined by CHNS analyzer

[c]Estimated by BET approach

[d]Estimated by BJH approach

in Table 1. XRF results were confirmed a little drop in the actual contents of nickel oxide was occurred compared to theoretical values for the fresh catalysts, which were in a good accordance with the literature [42–47]. This is because the segment of nickel metal was not precipitated on the supports during the catalyst's synthesis [42–45].

XRD results

The phase structure of the calcined catalysts was analyzed using XRD test, and the results are shown in Fig. 1. The XRD patterns exhibited characteristic peaks for γ-alumina at $2\theta = 45.1°$ and $66.4°$ in all the samples, regardless of NC catalyst [48].

Furthermore, the XRD patterns of the synthesized catalysts, except for the NA catalyst, displayed three high-intensity diffraction peaks at 2θ values of $28.4°$, $56.4°$, and $79.4°$, corresponding to the cubic fluorite structural cerium oxide based on the JCPDS standard card [49]. Variations in the intensity of these peaks were observed with changes in ceria content in the catalysts with hybrid supports. The intensity of these characteristic peaks was augmented by elevating the ceria content in the catalysts with the hybrid supports, while the intensity of γ-alumina diffraction peaks decreased with higher ceria loading in the hybrid support. It is noteworthy that the positions of the peaks belonging to alumina and cerium oxide were consistent in the XRD patterns of all fresh catalysts (see Fig. 1). Prior studies have indicated that the γ—alumina crystal phase transforms into θ—alumina or α—alumina after calcination of catalysts supported on the γ—alumina was performed at temperatures exceeding 800 °C, resulting in reduced surface area and catalytic activity [50–53]. Therefore, addition of CeO$_2$ stabilizes and
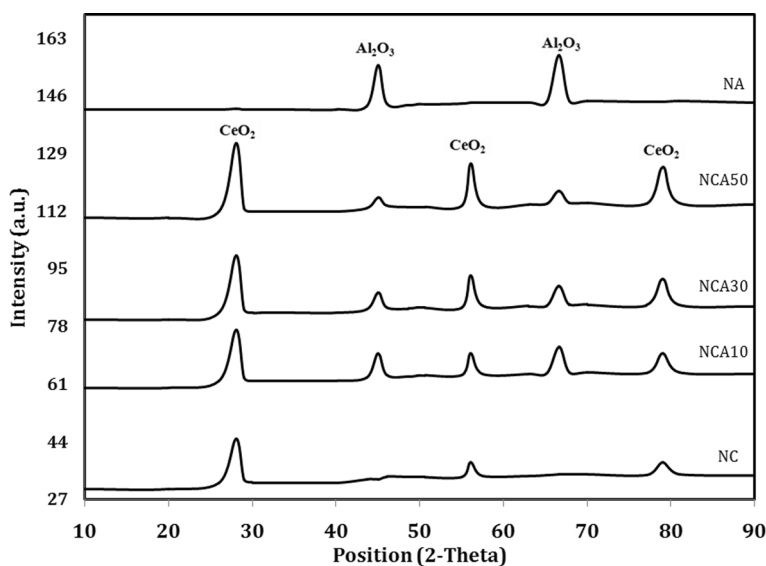

Fig.1 XRD profiles of the fresh catalysts

prevents the phase change of γ—alumina, thereby modifying the thermal stability and catalytic activity of catalysts supported on CeO_2–Al_2O_3 [51–54]. The diffraction peaks belonging to $NiAl_2O_4$ did not appear in XRD patterns of NA, NCA10, NCA30 and NCA50 catalysts, indicating that the crystal size of $NiAl_2O_4$ was too small to be easily detected by XRD analysis. This finding is consistent with results reported by various researchers studying catalysts supported on Ce–Al_2O_3 support [55–57]. However, Dekkar et al. [29] reported that the $NiAl_2O_4$ spinel structure appears at the same position as Al_2O_3, suggesting their overlap in the XRD spectrum of Ni/Al_2O_3 catalyst.

He et al. [58] demonstrated that no characteristic peaks assigned to NiO or $NiAl_2O_4$ were detected in XRD profiles of Ni/Ce–Al_2O_3 catalysts, suggesting that metal species were highly dispersed on the Ce–Al_2O_3 support, preventing metal sintering. While, crystalline phases corresponding to nickel oxide may exist in the XRD spectra of fresh catalysts, characteristic peaks of NiO were not observed in the XRD spectra of the synthesized catalysts, suggesting that the crystal size of nickel oxide is very small (less than 3 nm) and not easily detected by XRD test. Similar results were reported by Jiao et al. [59] and Mosayebi et al. [47] using Ni, Co, Ni–Zn, Ni–Co and Ni–Fe catalysts supported on the Ce–Al_2O_3. The XRD patterns of the reduced catalysts were shown in Fig. 2. The main diffraction peaks in the XRD patterns of the reduced catalysts included γ–Al_2O_3 (regardless of NC catalyst), CeO_2 (regardless of NA catalyst) and metallic nickel (see Fig. 2). For reduced catalysts, the position of the peaks related to γ–Al_2O_3 and CeO_2 did not shift compared to those corresponding to the fresh catalysts (see Figs. 1 and 2). In the XRD profile of the catalysts after reduction treatment, the main phases attributed to metallic nickel appeared at 45.3° and 76.3° [60–63].
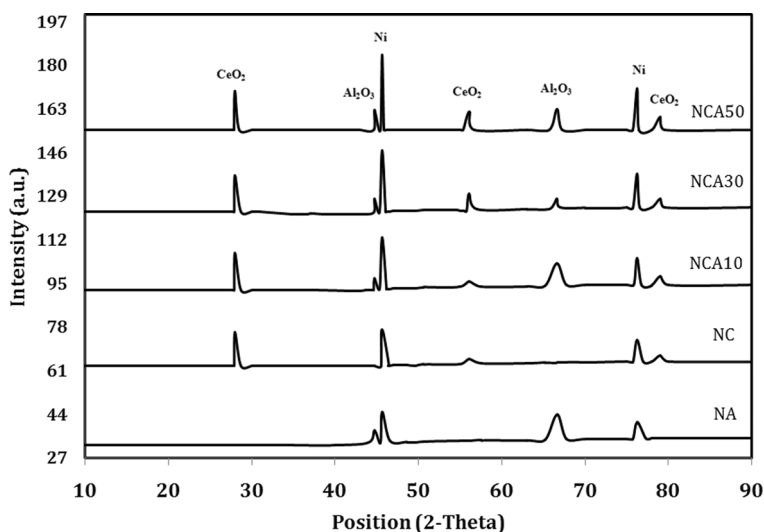

Fig.2 XRD patterns for the reduced catalysts

Textural properties

The physicochemical properties of nickel catalysts supported on Al$_2$O$_3$, CeO$_2$ and Al$_2$O$_3$–CeO$_2$, including pore volume, surface area, and average pore diameter were shown in Table 1. NA catalyst recorded a surface area of around 151.32 m^2 g^{-1} after calcinations treatment, while this value for NC catalyst measured 175.34 m^2 g^{-1}.

The surface area values for NCA catalysts ranged from 151.32 to 175.34 m^2 g^{-1}. The addition of ceria and formation of hybrid support increased the values surface area values of Ni-based catalysts in the order: NC > NCA50 > NCA30 > NCA10 > NA. Generally, the surface area values were augmented by increasing ceria content in the hybrid support. The similar results were observed for pore volume values of the synthesized catalysts.

H$_2$-TPR

H$_2$-TPR patterns of the prepared catalysts were shown in Fig. 3. The H$_2$-TPR test was conducted to investigate the reduction behavior and determine the optimal reduction conditions.

As shown in Fig. 3, the NA catalyst exhibited noticeable hydrogen consumption with two peaks at approximately 445 and 843 °C, attributed to the reduction of NiO and NiAl$_2$O$_4$ species, respectively [41]. The high-temperature hydrogen consumption peak was associated with the reduction of nickel oxide species that interacted remarkably with the alumina support [37]. Previous studies have indicated that the nickel oxide reduction peaks typically occur in the range of 340–450 °C, while the hydrogen peak for NiAl$_2$O$_4$ is observed at 700–850 °C [39, 41]. As shown in Fig. 3, three evident hydrogen consumption peaks were detected in the TPR patterns of NCA10, NCA30 and NCA50 catalysts. These peaks were located in the temperature
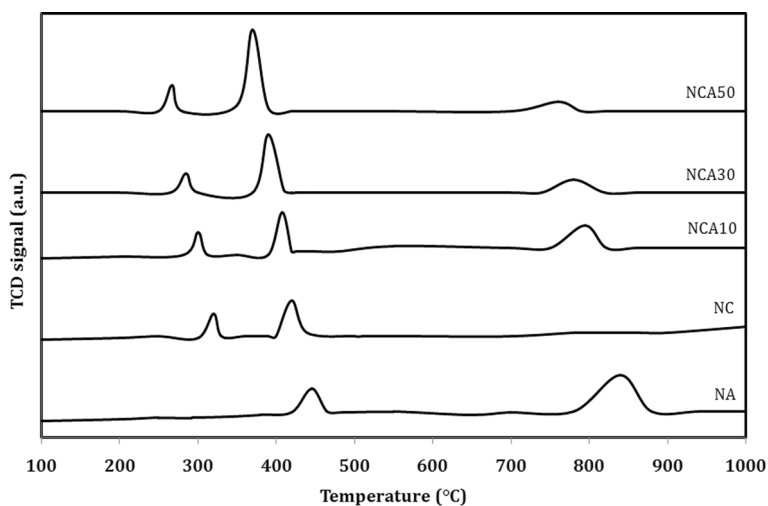

Fig.3 H$_2$-TPR results for all samples

ranges of 240–350 °C, 390–450 °C and 750–850 °C corresponding to the reduction of CeO_2 species to CeO_x, nickel oxide to metallic nickel and $NiAl_2O_4$ species, respectively [47].

For NC catalyst, two hydrogen peaks were observed in the TPR profile, which attributed to the reduction of CeO_2 species to CeO_x and nickel oxide to metallic nickel, respectively. Several studies have reported the presence of two distinct peaks in the temperature ranges of 250–350 °C and 600–900 °C in the TPR patterns of catalysts supported on Ce–Al_2O_3, which are associated with the reduction of CeO_2 species [37, 47]. Increasing the loading of cerium oxide in hybrid supports resulted in the shifting of the positions of CeO_2, NiO, and $NiAl_2O_4$ species reduction peaks to lower temperatures, thereby facilitating the reduction of the synthesized catalysts [47]. It was observed that the intensities of the reduction peaks related to $NiAl_2O_4$ species decreased with higher ceria content in the catalysts supported by hybrid materials, indicating a reduction in the interaction between the alumina support and nickel species. Conversely, the intensity of NiO hydrogen consumption peaks followed the order: NCA50 > NCA30 > NCA10 > NC > NA.

The values of hydrogen consumption as well as reduction degree were determined through TPR analysis in the temperature range of 240–500 °C, and were shown in Table 2. The values of hydrogen consumption and reducibility of NA and NC catalysts were 0.000107 mol and 61.4%, 0.000118 mol and 68.76%, respectively. This indicates that NC catalyst has a higher number of accessible nickel active sites than the NA catalyst for reactants compared to the NA catalyst, leading to improved catalytic [45].

The values of hydrogen consumption and reducibility were augmented by raising the loading of ceria in the hybrid support. The maximum values of hydrogen consumption and reduction degree were 0.000141 mol and 84.5%, respectively, observed for the NCA50 catalyst.

H_2-chemisorption

The results of H_2-chemisrption analysis, including nickel dispersion and average particle size were shown in Table 3. The nickel dispersion and average particle size of the reduced NA, NC, NCA10, NCA30 and NCA50 catalysts were calculated as 15.55% and 6.17 nm, 12.24% and 7.84 nm, 10.08% and 9.52 nm, 8.71% and 11.02 nm, 7.52% and 12.75 nm, respectively. Consequently, the nickel average particle size increased with the formation of hybrid supports and with higher loading of

Table 2 The values of hydrogen consumption and reducibility of synthesized catalysts

Sample	H_2 consumption (mole)	Reducibility (%)
NA	0.000107	61.4
NC	0.000118	68.76
NCA10	0.000127	73.4
NCA30	0.000136	78.3
NCA50	0.000141	84.5

Table 3 The results of H$_2$-chemisorption analysis and XRD test

Sample	Nickel dispersion (%)[a]	Nickel average particle size (nm)[b]	Nickel average particle size (nm)[c]
NA	15.55	6.17	5.24
NC	12.24	7.84	6.02
NCA10	10.08	9.52	8.02
NCA30	8.71	11.02	9.45
NCA50	7.52	12.75	10.57

[a]Dispersion = 100 × number of metallic nickel atoms on the surface/total number of metallic nickel atoms

[b]Nickel size was measured by H$_2$-chemisorption using 96/ dispersion

[c]Nickel size was measured by from the XRD profiles of the reduced catalysts using the Debye–Scherrer equation at 45.3°

cerium oxide in the catalysts with the hybrid supports. The highest and lowest average particle size were observed for NCA50 (12.75 nm) and NA (6.17 nm), respectively. However, the reverse results were obtained for nickel dispersion. The average particle size was calculated through H$_2$-TPD analysis was bigger compared to values derived from XRD patterns of reduced catalysts, indicating partial blockage of nickel by support species leading to a reduction in H$_2$-chemisorption to some extent [7, 39].

Catalytic tests

Catalytic activity

The CO$_2$ conversion, CO selectivity and CH$_4$ selectivity from 240 to 400 °C were shown in Figs. 4a, b & c, respectively. As shown in Fig. 4a, CO$_2$ conversion was increased by increasing the temperature. The CO$_2$ conversions were higher than the thermodynamic equilibrium values for the RWGS reaction at atmospheric pressure, indicating that the CO$_2$ methanation reaction is the predominant reaction over the RWGS reaction [49, 50]. Ni supported on CeO$_2$ exhibited higher CO$_2$ conversion compared to Ni supported on alumina catalyst. The addition of CeO$_2$ to NA catalyst and the formation of Ni/CeO$_2$–Al$_2$O$_3$ catalysts led to an increase in CO$_2$ conversion. The higher values of CO$_2$ conversion for NC catalyst compared to NA catalyst were related to their enhanced alkaline nature, oxygen vacancy and Ni species on the catalysts surface [38]. The H$_2$-TPR analysis (see Fig. 3) revealed that the peak related to NiAl$_2$O$_4$ spinel was relatively large in NA catalyst, indicating fewer Ni available for the CO$_2$ methanation reaction compared to NCA10, NCA30, and NCA50 (see Fig. 3). Consequently, NA catalyst exhibited lower catalytic performance compared to NCA10, NCA30, and NCA50. The lower interaction of Ni species with supports containing CeO$_2$–Al$_2$O$_3$ was confirmed by TPR analysis (see Fig. 3). The lower interaction leads to access more nickel species for reactants and is major reason for the superior catalytic activity of catalysts supported on CeO$_2$–Al$_2$O$_3$. The
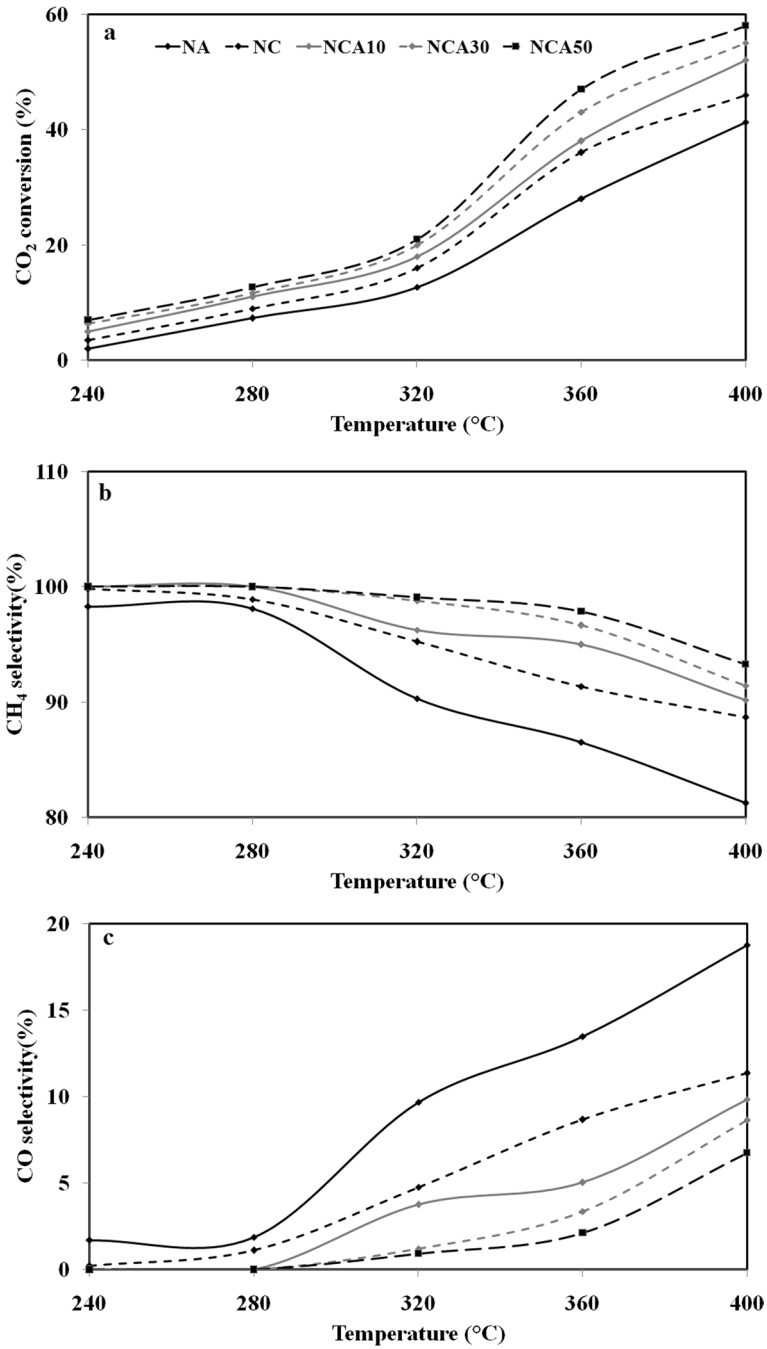
Fig.4 **a** CO_2 conversion, **b** CH_4 selectivity and **c** CO selectivity of NA, NC, NCA10, NCA30 and NCA50 catalysts

order of hydrogen consumption for the catalysts was NCA50 > NCA30 > NCA10 > NC > NA, indicating that a higher hydrogen consumption corresponds to a higher number of accessible nickel active sites and consequently higher catalytic activity (see Table 2). According to Fig. 4a, NCA50 catalyst showed highest CO$_2$ conversion at all temperatures, reaching a CO$_2$ conversion of 58% at 400 °C. The increase in available Ni species on the catalysts surface led to little decline in Ni dispersion and an increase in Ni particle size in NCA10, NCA30 and NCA50 compared to NA and NC catalysts (see Table 3). However, since Ni loading was maintained at a low level of 5 wt.% in all catalysts, and CeO$_2$ containing catalysts exhibited specific surface areas higher than 140 m^2 g^{-1}, this increase in Ni particle size (less than 6 nm) or decrease in Ni dispersion wasn't significant and didn't affect their catalytic activity. The enhancement of CO$_2$ adsorption by basic sites of support overcame the increase of Ni particle size effect. The synergetic effect between nickel active sites and CeO$_2$-Al$_2$O$_3$ improved the metal-support interaction, resulting in higher catalytic performance and durability of catalysts.

The increase in Ni dispersion or decrease in Ni particle size can be achieved by the addition of alkali or rare earth metal as promoter to Ni [64]. Several researchers have reported an increase in oxygen vacancy, nickel active sites, and a decrease in particle size by adding CeO$_2$–Al$_2$O$_3$ support [25, 47, 58, and 59]. Wu et al. [25] declared that number of oxygen vacancies on the catalyst surface augmented with augmenting ceria content in Ni/Al$_2$O$_3$ catalyst using X-ray photoelectron spectroscopy (XPS) analysis. The alkaline nature of CeO$_2$ produced a high percentage of basic sites, enhancing CO$_2$ adsorption and facilitating CO$_2$ activation [37]. Daroughgi et al. [46] promoted the 25%Ni/Al$_2$O$_3$ with 5 wt.% Ce, Zr, La and Mo. Ce promoted catalysts showed superior catalytic activity, which can be attributed to large amount basic sites [47, 48]. CO$_2$ methanation converts CO$_2$ to methane via "CO route" or "formate route" [51]. In the CO route, CO is the primary intermediate, which is consecutively transformed to methane through CO hydrogenation [51]. In the formate mechanism, formate is the main intermediate species interacting with dissociated hydrogen to produce methane. Ren et al. [41] suggested that CO route is the most probable mechanism for Ni-based catalysts as it was disclosed by density functional theory (DFT). In both proposed routes, an increase in adsorption of CO$_2$ is favorable for methanation reaction [41]. Wang et al. [20] promoted Ni/MCM41 by addition of 5 wt.% CeO$_2$ to Ni. Addition of CeO$_2$ as a promoter of Ni improved metal-support interaction and Ni dispersion [51]. The RWGS reaction, as the main side reaction of methanation reaction follows "redox" or "associative" mechanisms [12, 13]. Enhancement of CO$_2$ adsorption also promotes both of these mechanisms [13]. RWGS, due to its endothermic nature, is favored at higher temperatures, while the exothermic methanation reaction is preferred at lower temperatures [16]. At higher temperatures, CO$_2$ methanation and RWGS reactions become competitive [20]. This is the main reason for the increase in CO selectivity and decrease in CH$_4$ selectivity at higher temperatures (see Fig. 4b, c). Catalysts containing higher CeO$_2$ content showed higher CH$_4$ selectivity than CO selectivity, especially at temperatures exceeding 320 °C. The CH$_4$ selectivity of catalysts followed the following order at all temperatures: NCA50 > NCA30 > NCA10 > NC > NA, while the reverse trend was observed for CO selectivity. NCA50 showed CH$_4$ and CO selectivity of

93.26 and 6.74% at 400 °C, respectively. For the NA catalyst, a large amount of nickel was entrapped in the structure of $NiAl_2O_4$, which cannot be easily reduced. However for NCA10, NCA30 and NCA50 catalysts, the available Ni species on the catalysts surface were much higher than those entrapped in $NiAl_2O_4$. The higher availability of Ni species on the catalyst surface enhances the adsorption and dissociation of hydrogen [23]. In CO_2 methanation, each mole of CO_2 reacts with 4 mol of H_2 to produce CH_4. If there is not enough dissociated H_2, the carbon dioxide has a higher tendency for reaction with hydrogen via RWGS ($CO_2 + H_2 \leftrightarrow CO + H_2O$) than the methanation reaction. Tada et al. [55] evaluated 1, 3, 5 and 10 wt.% Ni/CeO_2 catalysts in CO_2 methanation reaction. They found that three types of active site were available: 1. metallic Ni surface, 2. oxygen vacancies on CeO_2 (Ce–Vox–Ce), and 3. Oxygen vacancies of Ni–Ce mixed oxides (Ni–Vox–Ce). Ni–Vox–Ce sites were more important at 1 and 3 wt.% and temperatures lower than 250 °C [55]. Some scholars synthesized Ni-based catalysts with loadings higher than 10 wt.% for CO_2 methanation to reach high nickel active site and H_2 dissociation [46, 51]. However, these catalysts suffer from low thermal stability, agglomeration, and sintering of Ni particles [46, 51]. At temperatures exceeding 400 °C, methane steam reforming reaction may also occur, leading to an increase in CO selectivity and a decrease in methane selectivity [51].

Catalytic stability

The stability test for prepared catalysts in the CO_2 hydrogenation reaction at a temperature of 400 °C was shown in Fig. 5. For the NA catalyst, CO_2 conversion remained stable without an obvious decrease during initial 35 h on stream, after which it gradually declined from 41.25 to 31.45% between 35 and 60 h (see Fig. 5a). CO_2 conversion of 70.43% was maintained for the initial 10 h using 25% Ni/Al_2O_3 catalyst at 350 °C [38]. The various reports have highlighted that the stability of Ni/
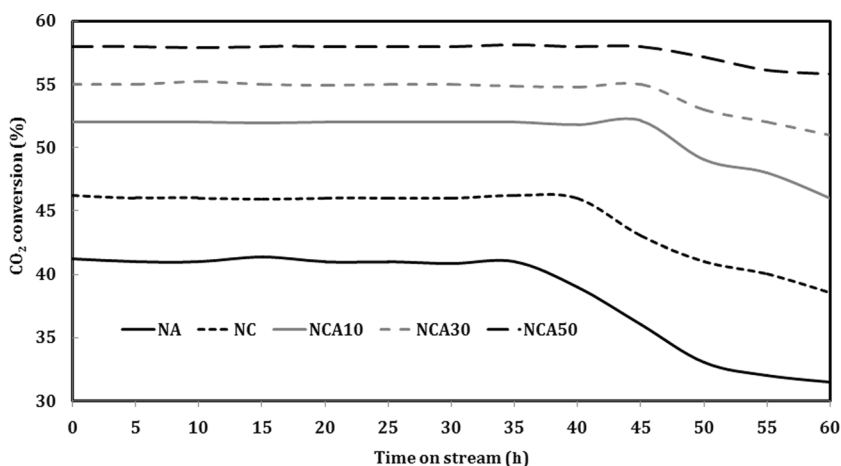

Fig.5 The stability test of spent catalysts in CO_2 hydrogenation reaction at 400 °C

Al$_2$O$_3$ and Co/Al$_2$O$_3$ catalysts in the CO$_2$ hydrogenation reaction varies, which is correlated with the dispersion of active metals, textural structure, and resistance to coke formation [46, 54]. Scholars have demonstrated that coke deposition on the catalyst surface during CO$_2$ hydrogenation is the principal factor leading to catalyst deactivation [56, 57]. As shown in Fig. 5, it is apparent that the stability of NC catalyst in the CO$_2$ hydrogenation reaction was higher compared to NA catalyst, as CO$_2$ conversion remained constant for the initial 40 h on stream. Furthermore, catalysts with the hybrid support exhibited higher stability, maintaining CO$_2$ conversion for approximately 45 h on stream without any loss, compared to the NA and NC catalysts (see Fig. 5a). After 45 h, a decrease in the CO$_2$ conversion was observed from 52.05 to 46.42%, 55.73 to 51.54% and 58.22 to 56.08% for NCA10, NCA30 and NCA50 catalysts, respectively. Thus, the loss in CO$_2$ conversion for the NCA50 catalyst was smaller compared to the other catalysts, indicating its higher stability in the CO$_2$ hydrogenation reaction and resistance to deactivation. This finding is consistent with the results obtained from TGA and CHNS analyzer (see Fig. 6 and Table 1).

Characterization of the spent catalysts

As shown in Table 1, the highest coke formation among the spent catalysts was observed for the NA catalyst. However, with the addition of ceria to the NA sample and the formation of hybrid support, the reduction in coke formation was mitigated during the stability test. The NCA50 catalyst exhibited the least carbon deposition after the stability test (see Table 1). Therefore, the coke deposition on the catalyst surface was decreased by increasing the ceria content in the catalysts with the hybrid supports.
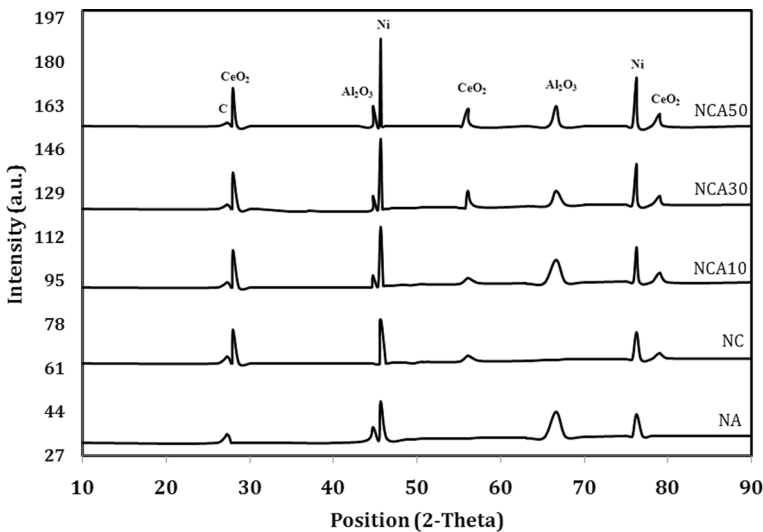

Fig.6 XRD patterns of the spent catalysts

The surface area and porosity of the spent catalysts were analyzed using N_2 adsorption–desorption test, and the results shown in Table 1. It was observed that coke deposition on the catalyst surface following the stability test led to suppression in surface area and porosity. The extent of loss in surface area and porosity enhanced with the amounts of deposited coke on the catalyst surface. The NA and NCA50 catalysts exhibited the maximum and minimum loss in porosity and surface area, respectively. Thus, it can be concluded that addition of ceria to Ni-based catalysts supported on alumina, along with an increase in ceria loading in hybrid supports, resulted in a reduction in surface area and porosity values. The results shown from Table 1 demonstrated that synergism between alumina and ceria in the hybrid supports enhanced durability against coke deposition on the catalyst after the CO_2 hydrogenation reaction. These findings were in a good accordance with others reports [62].

The diffraction patterns of the spent catalysts (for 70 h and at temperature of 400 °C) were shown in Fig. 6. In all spent catalysts, the main diffraction peaks in the XRD profiles included carbon, γ–Al_2O_3 (regardless of NC catalyst), CeO_2 (regardless of NA catalyst) and metallic nickel (see Fig. 6). For all spent catalysts, the carbon phase was detected at $2\theta = 27.2°$ [47, 60]. The positions of the peaks for metallic nickel, γ-Al_2O_3 and CeO_2 in the spent catalysts were consistent with those of the reduced catalysts (see Figs. 2 and 6). In agreement with the XRD patterns of calcined catalysts, the peaks corresponding to $NiAl_2O_4$ did not reveal in the XRD spectrum of fresh and spent catalysts due to the small crystal size of this phase. The average crystal size of metallic nickel was determined from the XRD profiles using the Debye–Scherrer equation at 45.3°. These values for spent NA and NC catalysts were 7.23 and 8.51 nm, respectively (see Table 4), while for the reduced NA and NC catalysts; they were 5.24 and 6.02 nm (see Table 3), respectively.

As seen in Figs. 2 and 6, the intensity of the peaks of metallic nickel in the XRD patterns of used and reduced catalysts augmented and became narrower with the increasing ceria loading in the catalysts with hybrid supports. This indicates that the average crystal size of nickel increased with the raising ceria content in the catalysts with hybrid support. The average crystal sizes for metallic nickel in the spent NCA10, NCA30 and NCA50 catalysts were 9.82 nm, 11.34 and 14.07 nm (see

Table 4 The contents of hydrogen and carbon elements in the coke deposition

Catalyst	wt.% carbon	wt.% hydrogen	Carbon to hydrogen mole ratio	Nickel average particle size (nm)[a]
NA	19.1	0.95	1.67	7.23
NC	17.4	0.99	1.45	8.51
NCA10	15.6	1.02	1.27	9.82
NCA30	14.1	1.04	1.12	11.34
NCA50	12.8	1.13	0.94	14.07

[a]Nickel size was measured by from the XRD profiles of the spent catalysts using the Debye–Scherrer equation at 45.3°

Table 4), respectively, while for the reduced NCA10, NCA30, and NCA50 catalysts, they were 8.02, 9.45, and 10.57 nm (see Table 3), respectively. The diameter of nickel nanoparticles for the spent catalysts was larger compared to the reduced catalysts. As described in the previous section, the crystal phase belonging to nickel oxide did not appear in the XRD patterns of the fresh catalysts, indicating that nickel oxide particles sizes were very small, (smaller than 3 nm) because of low crystallinity or higher dispersion of nickel oxide particles on the support. The weight percentages of hydrogen and carbon in the coke deposition were determined using Element Analysis (EA), and the results were depicted in Table 4. It was clear that catalysts with higher coke deposition exhibited a higher quantity of carbon (see Tables 1 and 4). The mole ratio of carbon to hydrogen serves as an indicator of the aromaticity of the deposited coke on the catalyst surface [47, 64, and 65]. A higher mole ratio of carbon to hydrogen suggests that the coke is more aromatic, while lower values indicate a more aliphatic nature [47].

The NA catalyst demonstrated the highest mole ratio of carbon to hydrogen, indicating that the deposited coke was predominantly aromatic and less aliphatic. This ratio decreased for the NC catalyst compared to NA catalyst. In the case of catalysts with hybrid support, the mole ratio of C/H decreased with reduced coke formation on the catalyst surface, compared to the NA and NC catalysts. Among the catalysts with CeO$_2$–Al$_2$O$_3$ support, NCA50 exhibited a lower mole ratio of C/H than other catalysts, indicating that the deposited coke was highly aliphatic and less aromatic. Therefore, it can be concluded that the coke structure was more aliphatic for catalysts with lower coke formation after the CO$_2$ hydrogenation reaction (lower carbon to hydrogen mole ratio).

Figure 7 shows the results for TGA to assess the coke deposit on the catalysts surface after CO$_2$ hydrogenation. The NA catalyst displayed suitable thermal stability until 700 °C, with a weight loss of approximately 13% occurring in the temperature range of 700–1000 °C. Dekkar et al. [29] demonstrated that a mass loss in TGA patterns of Ni/Al$_2$O$_3$ catalyst beyond 600 °C could be attributed to the presence of graphitic carbon, known as the main factor responsible for catalyst deactivation in the dry reforming of methane. This is further confirmed by the XRD peak near 26°
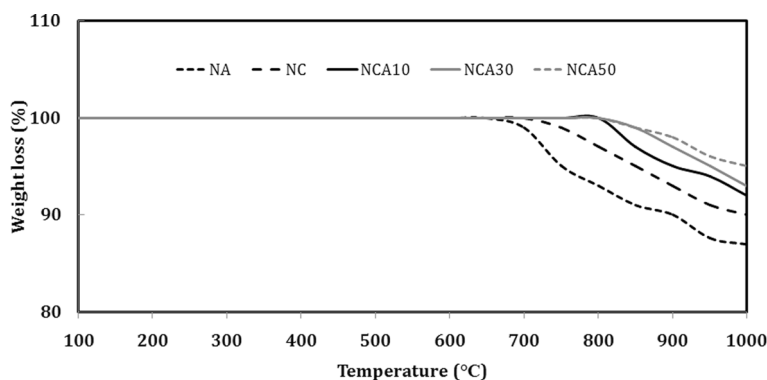

Fig.7 TG curves of catalysts after the durability test

(see Fig. 6). This may be related to the oxidation of deposited carbon on the spent catalysts' surface to form dioxide carbon. Wang et al. [66] described that catalyst deactivation caused by carbon formation on the catalyst surface depends on the type, amount, and position of the coke deposited. Some scholars [67, 68] observed two kinds of carbon species (graphitic and amorphous) on the surface of spent Ni-based catalysts in the dry reforming of methane. As shown in Fig. 7, the NC catalyst exhibited high thermal stability with no weight loss until 750 °C, followed by a gradual decrease of approximately 10% in the temperature range of 750–1000 °C. The weight losses near to 8, 7 and 5% were observed at temperatures exceeding 800 °C for the NCA10, NCA30 and NCA50 catalysts, respectively (see Fig. 7).

It is apparent that the thermal stability of catalysts with hybrid supports was higher compared to the NA and NC catalysts. Therefore, the thermal stability was enhanced by the addition of ceria to NA catalyst and also by increasing the cerium oxide content in the catalysts with hybrid support. Based on results of CHNS analyzer (see Table 1), the coking on the catalyst surface of NCA50 spent in the reaction was smaller than other catalysts (7.1 wt.%), which was in line with the stability test and TGA. The maximum coke deposited on the catalyst (9.8 wt.%) and weight loss of approximately 9% were assigned to the NA catalyst. The thermal stability and pyrolysis behavior of the coke species deposited on the catalyst surface were investigated using thermogravimetric and mass spectrometric (TG-MS) analysis in the presence of an N_2 gas stream. The results of this test were shown in Fig. 8. The structure of coke deposited on the catalyst surface can be studied by evaluating the amount and type of gaseous products released [47, 65]. The coke species exhibited distinct thermal stabilities, as shown in Fig. 8. The release of gaseous products corresponded to a drop in the weight of the coke. For the NC catalyst, a remarkable amount of CO_2 was released in the temperature range of 700–1000 °C, indicating the presence of carboxylic groups within the coke structure [65]. CO_2 was likely obtained from decarboxylation reaction during the coke pyrolysis [47, 65].

For the NA catalyst, the dioxide carbon peak exhibited three main ranges located at 200–400 °C, 500–700 °C and 700–1000 °C, whereas carbon dioxide was released in two ranges of 200–300 °C and 300–800 °C for NCA50 catalyst. The intensity of the hydrogen peak was also remarkable in the range of 800–1000 °C for both NC and NCA50 catalysts. The release of hydrogen gas is related to the dehydrogenation of saturated aliphatic or cyclic chains [29]. Additionally, a small amount of methane was released at 960 °C for the NC catalyst, suggesting the presence of methyl groups in the formed coke on the catalyst surface after the durability analysis [65].

Conclusions

The CO_2 hydrogenation reaction was evaluated using the 5%Ni/CeO_2–Al_2O_3 catalyst with varying ratios of CeO_2–Al_2O_3. CeO_2–Al_2O_3 hybrid support was prepared via deposition–precipitation method and nickel supported on the CeO_2–Al_2O_3, CeO_2 and Al_2O_3 using deposition–precipitation approach. XRD results of the fresh catalysts did not detect diffraction peaks corresponding to $NiAl_2O_4$ and NiO, likely due to their low crystallinity or higher dispersion of nickel particles. However,
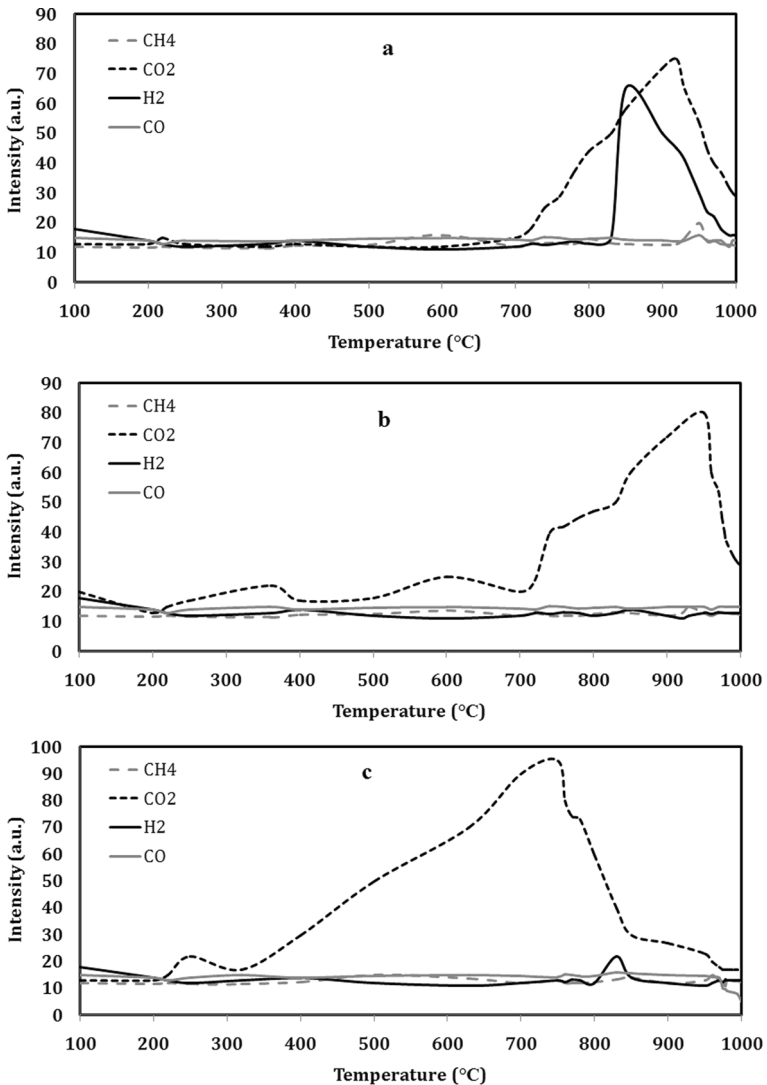
Fig.8 TG-MS curves of the catalysts after the durability test for different compounds, **a** NC, **b** NA, **c** NCA50 catalysts

dominant peaks related to metallic nickel were observed in the XRD patterns of spent catalysts, indicating an increase in particle size with higher ceria content in Ni/CeO$_2$–Al$_2$O$_3$ catalysts. The NA catalyst displayed high thermal stability until 700 °C, which improved to 800 °C with the introduction of ceria and formation of the hybrid supports, resulting in lower weight loss (less than 8%) for 5%Ni/CeO$_2$–Al$_2$O$_3$ catalysts. The Analysis using CHNS analyzer and EA revealed that coke deposition on the surface of the NCA50 catalyst was lower compared other catalysts. Furthermore, a lower mole ratio of carbon to hydrogen (0.94) indicated

a shift in coke structure from aromatic to aliphatic. The 5%Ni/CeO$_2$–Al$_2$O$_3$ catalysts with different CeO$_2$–Al$_2$O$_3$ ratios exhibited higher catalytic activity regarding to CO$_2$ conversion and methane selectivity compared to NA and NC catalysts. However, the reverse trend was observed for CO selectivity.

Author contributions Amir Mosayebi involved in conceptualization, methodology, validation, project administration, writing original draft, writing – review and editing, and supervision. Atieh ranjbar involved in methodology, writing original draft, writing –review and editing, and analysis data. Mohammad Hosein Eghbal Ahmadi involved in writing – review and editing, methodology, and analysis data.

Declarations

Competing interests The authors declare no competing interests.

References

1. A. Rafiee, J. Environ. Chem. Eng. **8**, 104314 (2020)
2. S. Chu, A. Majumdar, Nature **488**, 294 (2012)
3. S. Dekkar, Chem. Afr. **7**, 1 (2023)
4. A.A. Al-Absi, A. Domin, M. Mohamedal, A.M. Benneker, N. Mahinpey, Fuel **333**, 126401 (2023)
5. Y. Zhang, H. Liu, J. Qi, P. Feng, X. Zhang, D. Li Liu, G.W. Marek, R. Srinivasan, Y. Chen, Sci. Total. Environ. **857**, 159482 (2023)
6. X. Li, Y. Xia, Y. Xu, H. Li, J. Huang, J. Yao, H. Zhao, X. Gao, J. Yu, L. Guo, J. Li, Res. Chem. Intermed. **49**, 3933 (2023)
7. M. Mehrabi, M. Ashjari, F. Meshkani, Res. Chem. Intermed. **50**, 219 (2024)
8. A. Dyachenko, O. Ischenko, V. Diyuk, O. Goncharuk, M. Borysenko, O. Mischanchuk, Res. Chem. Intermed. **48**, 2607 (2022)
9. O.S. Joo, K.D. Jung, I. Moon, A.Y. Rozovskii, G.I. Lin, S.H. Han, S.J. Uhm, Ind. Eng. Chem. Res. **38**, 1808 (1999)
10. N. Bashiri, S.J. Royaee, M. Sohrabi, Res. Chem. Intermed. **44**, 217 (2018)
11. S.S. Kim, K.H. Park, S.C. Hong, Fuel Process. Technol. **108**, 47 (2013)
12. P. Shafiee, S.M. Alavi, M. Rezaei, Res. Chem. Intermed. **48**, 1923 (2022)
13. A. Goguet, F. Meunier, J.P. Breen, J. Catal. **226**, 382 (2004)
14. B. Lu, F. Quan, Z. Sun, F. Jia, L. Zhang, Catal. Commun. **129**, 105724 (2019)
15. X. Wang, H. Shi, J.H. Kwak, J. Szanyi, ACS Catal. **5**, 6337 (2015)
16. X. Zhang, X. Zhu, L. Lin, ACS Catal. **7**, 912 (2017)
17. F.M. Sun, C.F. Yan, C.Q. Guo, S.L. Huang, Int. J. Hydrogen Energy **40**, 15985 (2015)
18. M.A. Aziz, A. Jalil, S. Triwahyono, R.R. Mukti, Y.H. Taufiq-Yap, M.R. Sazegar, Appl. Catal B-Environ. **147**, 359 (2014)
19. Y. Bian, C. Xu, X. Wen, L. Xu, Y. Cui, S. Wang, C.E. Wu, J. Qiu, G. Cheng, M. Chen, Fuel **331**, 125755 (2023)
20. F. Hu, C. Jin, R. Wu, C. Li, G. Song, T.Z. Gani, K.H. Lim, W. Guo, T. Wang, S. Ding, R. Ye, Chem. Eng. J. **461**, 142108 (2023)
21. L. Wang, H. Liu, Y. Chen, S. Yang, Int. J. Hydrogen Energy **42**, 3682 (2017)
22. H.H. Shin, L. Lu, Z. Yang, C.J. Kiely, S. McIntosh, ACS. Catal. **6**, 2811 (2016)
23. L.R. Winter, R. Chen, X. Chen, Appl. Catal. B **245**, 360 (2019)
24. B. Lu, K. Kawamoto, Mater. Res. Bull. **53**, 70 (2014)
25. P. Shafiee, S.M. Alavi, M. Rezaei, Int. J. Hydrogen Energy **46**, 3933 (2021)
26. H.C. Wu, Y.C. Chang, J.H. Wu, Catal. Sci. Technol. **5**, 4154 (2015)
27. N. Martin, P. Velin, M. Skoglundh, M. Bauer, P. Carlsson, Catal. Sci. Technol. **7**, 1086 (2017)
28. A. Ranjbar, A. Irankhah, S.F. Aghamiri, J. Environ. Chem. Eng. **6**, 4945 (2018)
29. B. Zhao, B. Yan, Z. Jiang, Chem. Commun. **54**, 7354 (2018)

30. S. Dekkar, S. Tezkratt, D. Sellam, K. Ikkour, K. Parkhomenko, A. Martinez-Martin, A.C. Roger, Catal. Letter. **150**, 2180 (2020)
31. A. Mosayebi, A. Haghtalab, Chem. Eng. J. **259**, 191 (2015)
32. J.A. Loiland, M.J. Wulfers, N.S. Marinkovic, R.F. Lobo, Catal. Sci. Technol. **14**, 5267 (2016)
33. C.S. Chen, J.H. Lin, J.H. You, K.H. Yang, J. Phys. Chem. A **114**, 3773 (2009)
34. R.M. Belekar, Phys. Lett. A **395**, 127206 (2021)
35. C.S. Chen, W.H. Cheng, S.S. Lin, Appl. Catal. A- Gen. **238**, 55 (2003)
36. K. Liu, X. Xu, J. Xu, X. Fang, L. Liu, X. Wang, J. Carbon Dioxide Util. **38**, 113 (2020)
37. X. Wei, W. Su, Y. Shi, J. Wang, P. Lv, X. Song, Y. Bai, G. Xu, G. Yu, Int. J. Hydrogen Energy **58**, 128 (2024)
38. L. Yang, L. Pastor-Pérez, S. Gu, A. Sepúlveda-Escribano, T.R. Reina, Appl. Catal. B- Environ. **232**, 467 (2023)
39. Z. Wu, A. Mann, M. Li, S. Overbury, J. Phys. Chem. **119**, 7340 (2015)
40. Y. Xu, H. Wan, X. Du, B. Yao, S. Wei, Y. Chen, W. Zhuang, H. Yang, L. Sun, X. Tao, P. Wang, Fuel Process. Technol. **236**, 107418 (2022)
41. A. Haghtalab, J. Shariati, A. Mosayebi, React. Kinet. Mech. Catal. **126**, 1003 (2019)
42. G. De Piano, J.J. Gamboa, A.M. Condó, F.C. Gennari, Int. J. Hydrogen Energy **22**, 1007 (2024)
43. A. Mosayebi, Int. J. Energy Res. **46**, 12207 (2022)
44. A. Mosayebi, Fuel **334**, 126711 (2023)
45. A. Mosayebi, M. Nasabi, R. Abedini, Petrol. Sci. Technol. **37**, 2338 (2019)
46. A. Mosayebi, R. Abedini, J. Fuel. Chem. Technol. **46**, 311 (2018)
47. R. Daroughegi, F. Meshkani, M. Rezaei, Chem. Eng. Sci. **230**, 116194 (2021)
48. A. Mosayebi, M.H. Eghbal Ahmadi, M. Hamidizirasefi, Int. J. Hydrogen. Energy. **48**, 33098 (2023)
49. D. Batebi, R. Abedini, A. Mosayebi, Ind. Eng. Chem. Res. **60**, 851 (2021)
50. K. Stangeland, D. Kalai, H. Li, Z. Yu, Energy Proc. **1**, 2022–2027 (2017)
51. M. Zhu, Q. Ge, X. Zhu, Trans. Tianjin Univ. **26**, 172 (2020)
52. X. Wang, L. Zhu, Y. Liu, S. Wang, Sci. Total. Environ. **625**, 695 (2018)
53. S. Xu, F. Xie, H. Xie, G. Zhou, X. Liu, Chem. Eng. J. **375**, 122023 (2019)
54. K. Stangeland, K. Dori, L. Hailong, Y. Zhixin, Energy. Proc. **105**, 2022 (2017)
55. A. Mosayebi, M. Nasabi, Int. J. Energy Res. **44**, 5500 (2020)
56. S. Tada, H. Nagase, N. Fujiwara, R. Kikuchi, Energy. Fuels. **35**, 5241 (2021)
57. Y. Ma, J. Liu, M. Chu, J. Yue, Y. Cui, G. Xu, Catal. Letter. **152**, 872 (2022)
58. G. Zhou, H. Liu, K. Cui, H. Xie, Z. Jiao, G. Zhang, K. Xiong, X. Zheng, Int. J. Hydrogen. Energy. **42**, 16108 (2017)
59. Z. He, Y. Jiao, J. Wang, Y. Chen, J. Anal. Appl. Pyrol. **122**, 142 (2016)
60. A. Mosayebi, Int. J. Energy Res. **45**, 3288 (2021)
61. A. Mosayebi, J. Taiwan. Inst. Chem. E. **114**, 36 (2020)
62. M.H. Eghbal Ahmadi, A. Mosayebi, J. Taiwan. Inst. Chem. E. **127**, 32 (2021)
63. D. Batebi, R. Abedini, A. Mosayebi, Int. J. Hydrogen Energy **45**, 14293 (2020)
64. A. Mosayebi, Res. Chem. Intermed. **47**, 2951 (2021)
65. A. Mosayebi, M.H. Eghbal Ahmadi, Energy. **261**, 125254 (2022)
66. N. Bashiri, M.R. Omidkhah, H.R. Godini, Res. Chem. Intermed. **47**, 5267 (2021)
67. S. Wang, G.Q. Lu, Appl. Catal. A-Gen. **167**, 271 (1997)
68. Y. Xu, X. Du, J. Li, P. Wang, J. Fuel. Chem. Technol. **47**, 200 (2019)
69. S. Zhang, J. Wang, Catal. Commun. **9**, 995 (2008)